

Direct observation of incommensurate structure in Mo_3Si

Ahmet Gulec,^a Xiaoxiang Yu,^a Matthew Taylor,^b John H. Perepezko^b and Laurence Marks^{a,*}

^aDepartment of Materials Science and Engineering, Northwestern University, 2220 Campus Drive, Evanston, Illinois 60208, USA, and ^bDepartment of Materials Science and Engineering, University of Wisconsin–Madison, 1509 University Avenue, Madison, Wisconsin 53706, USA. *Correspondence e-mail: l-marks@northwestern.edu

Received 16 May 2016

Accepted 29 July 2016

Edited by W. F. Kuhs, Georg-August University Göttingen, Germany

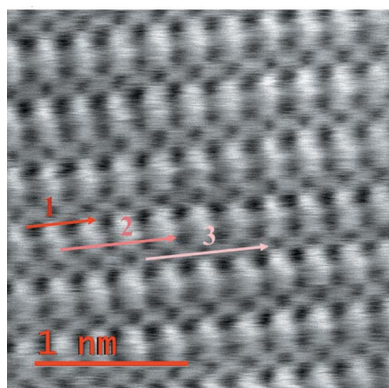
Keywords: Mo_3Si ; incommensurate structure; transmission electron microscopy; atom-probe tomography; electron diffraction.

Z-contrast imaging, electron diffraction, atom-probe tomography (APT) and density functional theory calculations were used to study the crystal structure of the Mo_3Si phase which was previously reported to have an A15 crystal structure. The results showed that Mo_3Si has an incommensurate crystal structure with a non-cubic unit cell. The small off-stoichiometry in composition of the sample which was revealed by APT and atomic resolution Z-contrast imaging suggested that site substitution caused the development of split atomic positions, disorder and vacancies.

1. Introduction

Topologically close-packed (TCP) or Frank–Kasper (FK) phase materials are the family of complex intermetallic compounds including a large number of materials with the A15 structure which have a composition of A_3B , where A is a transition metal (*e.g.* V, Nb or Mo) and B is from the right side of the periodic table (*e.g.* Al, Si, Ge and Sn). Many of these materials have attracted attention due to their superconducting properties and applications (Giorgi & Matthias, 1978; Giorgi *et al.*, 1978; Muller, 1980). Additionally, the superior mechanical properties of A15 structure materials have further applications such as in high-temperature alloys (Shah & Anton, 1992). For instance, it has been shown that Mo-based alloys are a good candidate for next-generation high-temperature applications with useful properties of strength and creep resistance, oxidation resistance and higher melting point (Perepezko, 2009; Dimiduk & Perepezko, 2003; Sakidja *et al.*, 2008). From neutron (Christensen *et al.*, 1983) and X-ray diffraction (Templeton & Dauben, 1950) it has been reported that Mo_3Si has a perfect A15 crystal structure in which the Si atoms are located at the corners and in the center of the cube (b.c.c., body-centered cubic), while the Mo atoms form mutually orthogonal linear chains that run throughout the crystal lattice. The available phase diagrams do not show any deviations from this ideal stoichiometry (Gokhale & Abbaschian, 1991).

In contrast, there are many other A15 alloys where there are substantial deviations from the ideal stoichiometry, for instance $\text{Mo}_{0.4}\text{Tc}_{0.6}$ (Giorgi & Matthias, 1978), $\text{V}_{0.29}\text{Re}_{0.71}$ (Giorgi *et al.*, 1978), $\text{W}_{0.6}\text{Re}_{0.4}$ and $\text{V}_{0.55}\text{Os}_{0.45}$ (Turchi *et al.*, 1983). In addition, some of the well studied materials with an A15 structure such as Nb_3Sn and V_3Si are reported to undergo a cubic-to-tetragonal structural transformation during cooling before the superconducting phase transition (Stewart, 2015). It has been reported that, in addition to this structural trans-



formation, a small tetragonal distortion and sublattice displacements occur from neutron scattering studies (Shirane & Axe, 1971) of Nb_3Sn and by EXAFS measurements of Nb_3Ge (Saini *et al.*, 2003). The nature of the structural transformations in the A15 materials is not necessarily the same; for instance the low-temperature tetragonal distortions ($c/a - 1$) are negative for Nb_3Sn while they are positive for V_3Si (Testardi, 1975).

Is Mo_3Si truly a single-phase material, or are there compositional and structural complexities similar to those found in some of the other A15 materials? What are the structural changes in these materials: just a small tetragonal distortion or something more complex? To date, one publication (Rosales & Schneibel, 2000) has suggested a slight off-stoichiometry where between 23.5% and 24% Si content the lattice parameter decreased with a slope of -0.0007 nm per at.% Si which was considered as being due to the smaller size of Si atoms compared to Mo atoms (Rosales & Schneibel, 2000). However, in order to determine the elemental composition they utilized a calculation of weight losses during the sample preparation and energy-dispersive X-ray spectroscopy (EDS), both of which can have relatively large errors for accurate compositional measurements.

In this paper we provide evidence that the non-stoichiometry in Mo_3Si is correct, and beyond that there is an incommensurate modulation, from direct observation of Mo_3Si by aberration-corrected electron microscopy, electron diffraction and atom-probe tomography (APT), combined with DFT (density functional theory) simulations. We suggest that many of the other A15 compounds could also have incommensurate modulations.

2. Experimental and computational details

Mo_3Si alloys were arc melted from 99.99% pure elemental reagents. Care was taken to ensure that the atom fractions of the Mo and Si were stoichiometric. The total ingot mass was nominally 10 g, and the ingot was melted and remelted five times to ensure homogeneity in a Ti-gettered environment; the ingot mass was measured between each melt to monitor losses or gains and ensure stoichiometry. The ingot employed in this study had a small 0.34% mass loss after the five remelts. The melting temperature of Mo_3Si , 2298 K, was exceeded on each remelt in a Ti-gettered atmosphere of Ar, and the melt was then allowed to fully cool on the hearth plate before airing the bell jar.

Transmission electron microscopy (TEM) and APT samples were prepared by lifting out specimens utilizing Ga^+ ion milling in an FEI Helios dual-beam focused ion beam (FIB) microscope. After liftout, the TEM samples were milled using low-energy and low-angle argon ions at 500 eV in a Fischione Model 1040 Nano-Mill to remove the amorphous and implanted layers. Atomic resolution scanning transmission electron microscopy (STEM) imaging was performed using an aberration-corrected JEOL ARM200CF with collection angles β of $11 \text{ mrad} \leq \beta \leq 22 \text{ mrad}$ for annular bright-field (ABF) imaging and $90 \text{ mrad} \leq \beta \leq 220 \text{ mrad}$ for high-angle

annular dark-field (HAADF) imaging which were acquired simultaneously. Electron diffraction experiments were performed utilizing a number of instruments, a JEOL ARM200CF, a JEOL 3010 with an LaB_6 emitter and a JEOL 2100F. A CAMECA Local Electrode Atom Probe (LEAP) 4000XSi with an ultrafast detector capability was used for the APT experiments. Picosecond pulses of ultraviolet laser light were utilized to evaporate individual atoms at a pulse repetition rate of 250 kHz, a laser pulse energy of 25 pJ per pulse and an average detection rate of 0.005 ions per pulse. The specimen tip temperature was maintained at 25 K. Data analyses were performed on the three-dimensional reconstructions of specimens utilizing the program *IVAS* 3.6.1 (CAMECA, Paris, France).

The stoichiometric Mo–Si compounds and their crystal structures were theoretically modeled using the evolutionary algorithm implemented in the USPEX code (Oganov & Glass, 2006) to determine the lowest-energy structures. Using such an approach eliminates bias introduced by selecting the structure manually and can allow for the discovery of phases not previously identified (Zhu *et al.*, 2012, 2013). This method performs a global optimization using a real-space representation and applying physical variation operators. For each candidate structure generated by USPEX, DFT calculations were performed at 0 K utilizing the *Vienna Ab-initio Simulation Package (VASP)* (Kresse & Hafner, 1993; Kresse & Furthmüller, 1996). The compounds explored in this work contained up to 30 atoms in the unit cell. The first generation consisted of 50 structures produced randomly. All the other generations contained 40 structures; of these, 40% of the new structures were produced by heredity, 20% produced by soft mutation, another 20% produced by transmutation and the final 20% produced randomly. Thermodynamically stable structures were determined by a convex hull construction where a phase is stable if its decomposition enthalpy into any other structures is positive (Tang *et al.*, 2004). The calculation was terminated when the stable structures did not change for ten generations. The *VASP* simulations utilized the projector augmented wave method (Kresse & Joubert, 1999; Blöchl, 1994) in conjunction with the generalized gradient approximation (GGA) using the parameterization by Perdew, Burke and Ernzerhof (PBE) (Perdew *et al.*, 1996). Plane waves with a cut-off energy of 600 eV and a k -point mesh (Monkhorst & Pack, 1976) resolution in reciprocal space of $2\pi \times 0.03 \text{ \AA}^{-1}$ yielded converged results. In addition to the evolutionary algorithm, due to the complexity of the incommensurate structures, supercells containing 512 atoms with random Mo substitution for Si were also calculated to compare with both global structural optimization and experimental observations.

3. Results

An atomic resolution HAADF image of Mo_3Si which shows only the Mo atomic columns for the [110] pseudo-cubic crystallographic orientation is shown in Fig. 1 with a magnified image and cartoon image of the perfect A15 structure for this particular orientation. In the magnified image in Fig. 1(b) the

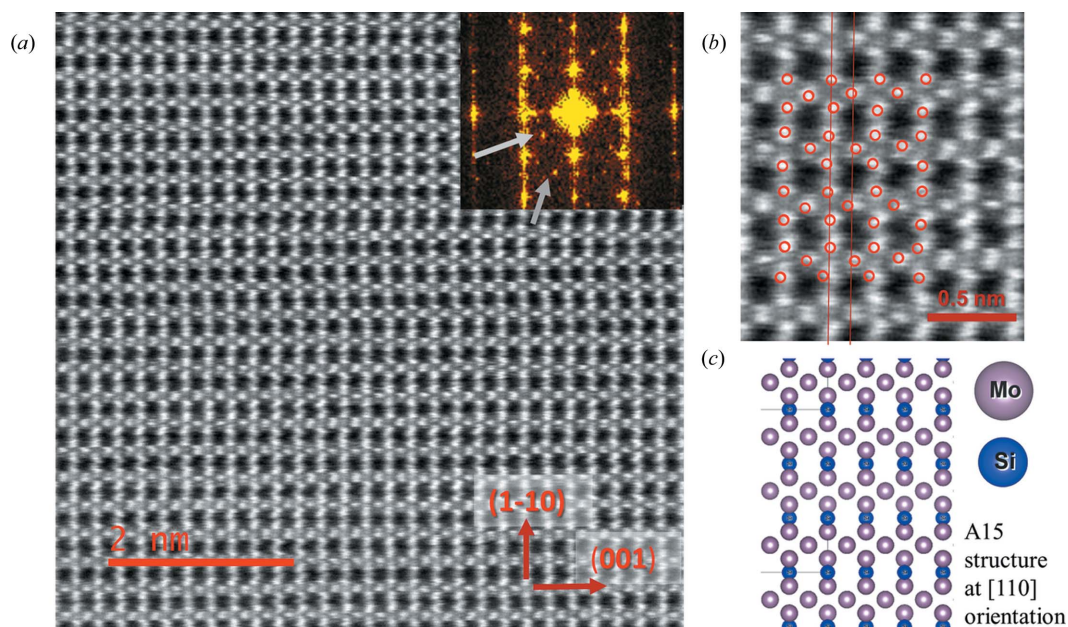


Figure 1
Atomic resolution HAADF image (a), (b) with FFT of the image inserted and a cartoon representation of atomic columns (c).

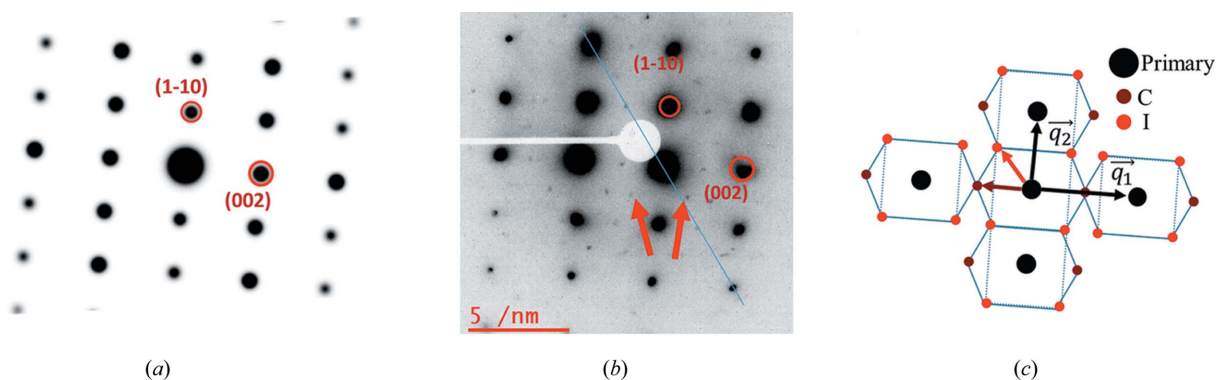


Figure 2
Kinematical simulation of the SAED pattern of perfect A15 structure in the [110] orientation (a) and the experimental result of Mo₃Si in the same crystallographic orientation (b), graphical illustration of the experimental results in which black dots are the primary reflection with a commensurate (C) and incommensurate (I) extra reflection which A15 symmetry does not have as shown in (c).

positions of the Mo atomic columns are labeled for which distortions of the atomic positions with respect to the perfect A15 symmetry are clearly shown. A fast Fourier transform (FFT) of the HAADF image shows an extra reflection indicated by the arrow in reciprocal space in Fig. 1(a). The kinematical selected-area electron diffraction (SAED) simulation of the perfect A15 structure for the pseudo-cubic [110] is shown in Fig. 2(a) for comparison with the experimental result, with the dynamic range modified to make the extra diffraction spots seen in Fig. 2(b) visible. The extra reflection spots are not expected for the perfect A15 structural symmetry as shown in the kinematical simulation. The periodic weak reflections can be classified into two groups, namely *commensurate* (C) and *incommensurate* (I) in addition to the primary reflections seen in Fig. 2(c). For the sake of simplicity,

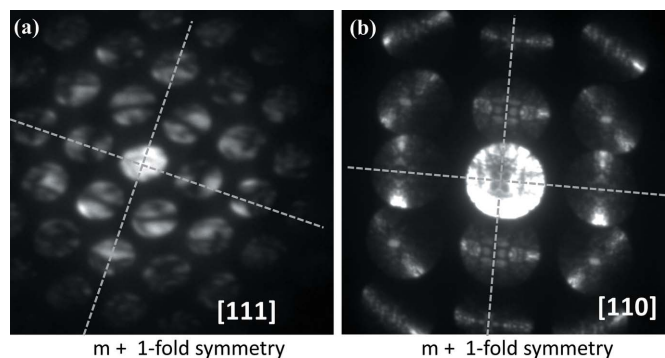
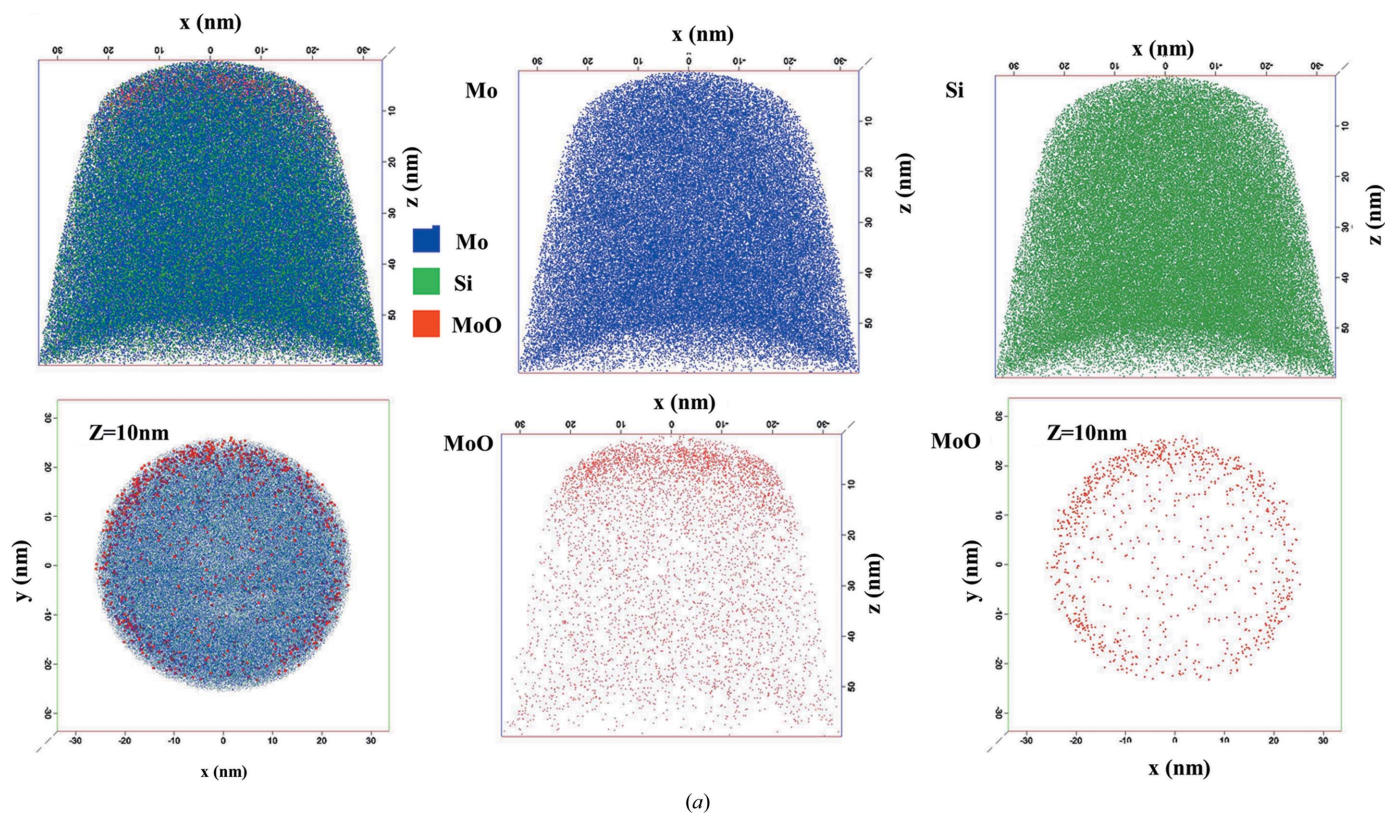


Figure 3
CBED pattern of Mo₃Si taken from the same grain for the [111] and [110] orientations and the relevant mirror symmetries.



(a)

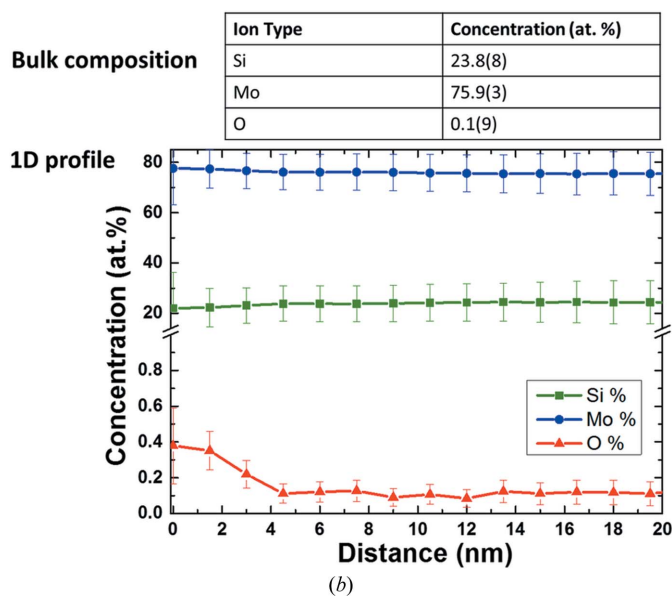


Figure 4
 (a) Three-dimensional APT reconstruction of the Mo_3Si tip with bulk composition with radial distribution at $z = 10$ nm and (b) one-dimensional concentration profile from the surface ($20 \times 20 \times 20$ nm tube region of interest).

one can define two vectors in reciprocal space which can span the whole space and define the major reflections, *i.e.* \mathbf{q}_1 and \mathbf{q}_2 as shown in Fig. 2(c) where $\mathbf{q}_1 = 2\mathbf{a}^*$, $\mathbf{q}_2 = (|\mathbf{a}^*|^2 + |\mathbf{b}^*|^2)^{1/2}(\mathbf{a}^* - \mathbf{b}^*)$ with \mathbf{a}^* and \mathbf{b}^* the unit vectors in reciprocal space of the primary reflections in the pseudo-cubic

coordinate system [100] and [010] directions, respectively. The commensurate spots are defined as $C = n\mathbf{q}_1/2$, where $n \in \mathbb{Z}$, and incommensurate modulation reflections can be written as $I = (1/2)\{[(n(2^{1/2}))/2]\mathbf{q}_1 + m\mathbf{q}_2\}$ where $n, m \in \mathbb{Z}$. The incommensurate modulations cannot be written as rational fractions of the primary reflections. Additionally, a straight line passing through one of the extra spots and the undiffracted central spot does not intercept with any major diffraction spot as seen by the blue line in Fig. 2(b). The commensurate reflections include kinematically forbidden (00ℓ) , $\ell = (2n + 1)$ reflections. These can occur for a range of reasons including dynamical diffraction as well as reduced symmetry due to site substitution and transitions from cubic to tetragonal or monoclinic structures. The primary reflections can be used to determine the major unit-cell parameters. SAED patterns were taken along the pseudo-cubic [111], [110] and $[1\bar{1}\bar{2}]$ crystallographic directions of the same grain to determine the unit-cell parameters. The results show that $a = b = 0.4898$ nm and $c = 0.4966$ nm with $\alpha = \gamma = 90^\circ$, $\beta = 90.5^\circ$,

To determine the structural symmetry, convergent-beam electron diffraction (CBED) patterns which are capable of providing much more information on the symmetry were acquired for the [111] and [110] pseudo-cubic crystallographic orientations of the same grain as shown in Fig. 3. For both directions, two mirror symmetry operations as well as a onefold rotational symmetry were found. The CBED results indicate that, based on the primary reflections, the highest crystal symmetry is monoclinic $2/m$ for the A15 structure; $Pm\bar{3}n$ symmetry was not observed.

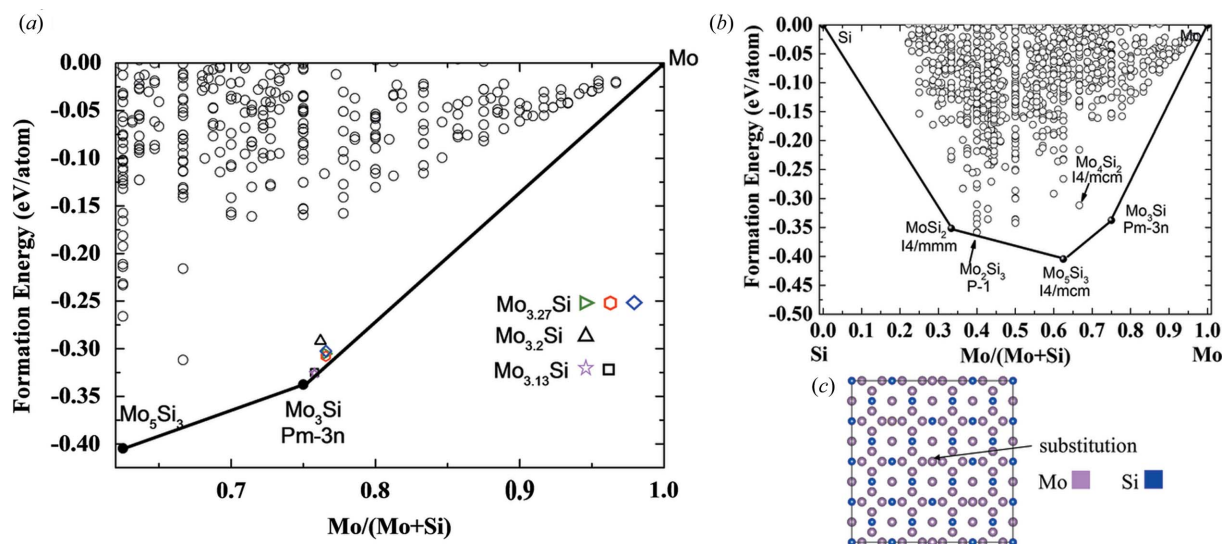


Figure 5

(a) The convex hull construction of the Si–Mo system at ambient pressure close to the Mo_3Si composition rate. Circles denote different structures; filled circles located on the convex hull are thermodynamically stable and are labeled in the figure; the open circles represent structures with higher energy. The energies of manually created substitutional models, labeled by colored shapes (Mo rich, 512 atoms in the supercell), are very close to those of the convex hull. (b) The full range of the convex hull construction of the Si–Mo system at ambient pressure. (c) Graphical representation of the manually created large unit cell with site substitution at the normal Si site.

It has been reported that the crystal structure of Mo_3Si is strongly dependent on small changes in the stoichiometry of the alloy (Rosales & Schneibel, 2000). APT has one of the highest accuracies for chemical composition with sub-nanometre spatial resolution. The APT results are shown in Fig. 4, indicating that the alloy is slightly off-stoichiometric such that the Mo/Si atomic ratio is 3.18 (23.88% Si) with a homogeneous Mo and Si distribution. The radial chemical distribution at $z = 10$ nm is also provided in addition to the residual surface oxygen on top of the tip and on the sides which is a result of reaction with oxygen in air after the APT tip was prepared.

To check the existence of a stable or metastable crystal structure in the Mo–Si systems, the results of the global DFT search are given in Fig. 5. In addition to the stoichiometric A15 structure, DFT calculation finds other stable phases MoSi_2 and Mo_5Si_3 and some metastable phases such as Mo_2Si_3 and Mo_4Si_2 , which do not exist in the phase diagram reported in the literature (see Fig. 5b). Of particular relevance here, the formation energies of three of the manually created supercells including $\text{Mo}_{3.13}\text{Si}$ (which has a composition close to that found by APT) are very close (<0.01 eV per atom) to the convex hull as shown in Fig. 5(a). This strongly suggests that the incommensurate modulation is due to Mo substitution at the Si sites in the A15 structure, as shown in Fig. 5(c).

In addition to determining the shape and size of the unit cell, the substitutional disorder was studied utilizing atomic resolution HAADF and ABF imaging as shown in Fig. 6. For collection angles greater than 90 mrad, HAADF images give Z -contrast information where the effect of diffraction contrast can be largely ignored and stronger signals represent heavier atomic columns in projection. This contrasts with the ABF image which can detect atoms with low Z numbers while darker areas are not necessarily representative of heavier

atoms (Okunishi *et al.*, 2012). Simultaneously obtained ABF and HAADF images which show the Mo atomic columns of Mo_3Si in pseudo-cubic $[110]$ orientation are shown in Figs. 6(a) and 6(b), respectively. In the ABF image, the periodic change in the pseudo-cubic $[1\bar{1}0]$ direction is labeled and shown with three arrows in Fig. 6(a). Arrow 1 and arrow 2 are positioned along the two atomic rows which are crystallographically equivalent to each other while the third arrow is different from the others. Keeping in mind that the contrast variations in ABF images are not necessarily an indication of compositional variations, the HAADF image which is taken simultaneously also displays a similar feature (see Fig. 6b). Also, intensity line scans from the HAADF image in the pseudo-cubic $[1\bar{1}0]$ direction are shown in Fig. 6(c) for row 1 only and in Fig. 6(d) for row 1 and row 2 combined with color coding. Fig. 6(c) clearly shows a periodic change in the atomic columns such that Mo atomic column pairs which are crystallographically equal have one small and one brighter contrast which is consistent with the ABF contrast variation. Moreover, the variation in the Mo atomic columns in position 3 does not show a periodic nature. Having different contrast at crystallographically equivalent columns in a Z -contrast image is a clear indication of site substitution between Si and Mo or vacancies; the DFT results and the stoichiometry suggest site substitution.

4. Discussion

Structural phase transition through cooling and structural distortions has been reported for materials with A15 symmetries, and the structural anomalies are attributed to different sources varying from hydrostatic pressure to point defects such as vacancies and site substitutions and stoichiometric variations (van Reuth & Waterstrat, 1968; Wang *et al.*,

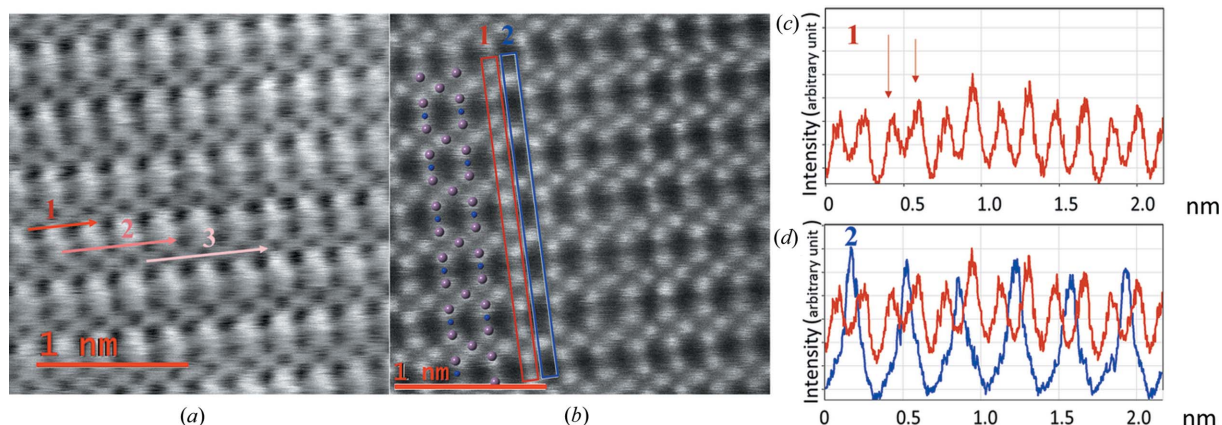


Figure 6
Atomic resolution ABF (a) and HAADF (b) images with the intensity line scans through the indicated directions (c), (d).

1982, 1986; Blaugher *et al.*, 1969; Tsutomu & Yasushige, 1983). Weak commensurate modulations at (00ℓ) , ℓ odd, seen in the diffraction pattern which are kinematically forbidden for a thin A15 specimen can be observed due to the tetragonal structure or site substitution stemming from changes in the form factor. Pseudo-tetragonality of the structure is confirmed by the diffraction pattern taken at different crystallographic orientations; however the effect of site substitution cannot be confirmed solely by diffraction. A tetragonal structure into which A15-type Nb_3Sn transforms through cooling (Shirane & Axe, 1971) provides the commensurate reflections in reciprocal space without any need for stoichiometric alteration. However, it neglects the triclinic structure obtained experimentally where β is slightly greater than 90° . Simulating the structural stability for small levels of off-stoichiometry is difficult since it requires excessively large supercell sizes.

Calculating the additional incommensurate modulation is much more difficult as it is observed in various metallic elements under different pressure (McMahon & Nelmes, 2006). In more complex phases such as $\beta\text{-Mg}_2\text{Al}_3$ with 1168 atoms per unit cell, an incommensurate structure due to a large number of partially occupied sites which leads to split positions and structural disorder has been reported (Samson, 1965; Steurer, 2007). Atomic ordering in binary A15-type structures consisting of various transition metals was reported to have long-range disorder despite being close to the perfect $1/3$ atomic ratio which suggests some fraction of atoms interchange their position (van Reuth & Waterstrat, 1968). Therefore, one should expect this kind of site substitution in Mo_3Si as suggested in the HAADF imaging results. The disorder can easily lead to distortions such as a different orientation of structural units or rotations *etc.* which are inherently independent of the major A15 symmetry. We note as well that partial occupancy is expected to adjust the effective electron concentration.

Another approach to complex alloy structure is based upon packing asymmetric icosahedra into crystals using other polyhedra with a larger coordination number and atoms where the coordination polyhedra form a TCP structure or an FK phase, introduced by Frank & Kasper (1958) – this includes

A15, Laves phases, σ , μ , M, P, R *etc.* among which A15 has the simplest structure. In addition to the 27 known FK phases, it has been found recently that there are hypothetically 71 new FK phases by using up to 20 atoms in a reduced fundamental domain (Dutour Sikirić *et al.*, 2010). After comparing the major symmetry in Mo_3Si which excludes the incommensurate modulations, we found no match between those hypothetical structures and the one observed experimentally. Because of the small number of atoms in the fundamental domain used in these calculations, we did not expect to find lower symmetries in more complex systems which require a larger unit cell; the experimental results which are found in the A15-type Nb_3Sn transforms through cooling (Shirane & Axe, 1971) are still more realistic than any hypothetical symmetries. Therefore, one can consider the observed structure to be a distorted structure from the parent A15-type structure.

Mo-Si -based alloys are candidates for a new high-temperature alloy family which has a variety of engineering applications. In this work we studied the crystal structure of the Mo_3Si phase which was previously reported to have an A15 crystal structure by utilizing Z-contrast imaging, electron diffraction, APT and DFT calculation. Our results show that Mo_3Si has an incommensurate crystal structure with a non-cubic unit cell. The small off-stoichiometry composition of the sample which leads to site substitution or vacancies is the reason for the structural disorder. However, it is still an open question as to what the underlying source of the incommensurate modulation is in Mo_3Si .

Acknowledgements

The authors acknowledge support from ONR MURI ‘Understanding Atomic Scale Structure in Four Dimensions to Design and Control Corrosion Resistant Alloys’ (grant No. N00014-14-1-0675). This work made use of the JEOL JEM-ARM200CF in the Electron Microscopy Service (Research Resources Center, UIC). The acquisition of the UIC JEOL JEM-ARM200CF was supported by an MRI-R2 grant from the National Science Foundation (DMR-0959470). Atom-probe tomography was performed at the Northwestern

University Center for Atom-Probe Tomography (NUCAPT). The authors are also grateful for technical discussions with Dr Dieter Isheim. Computations were performed using the Northwestern University's Quest high-performance computing cluster.

References

- Blaugher, R. D., Hein, R. E., Cox, J. E. & Waterstrat, R. M. (1969). *J. Low Temp. Phys.* **1**, 539–561.
- Blöchl, P. E. (1994). *Phys. Rev. B*, **50**, 17953–17979.
- Christensen, A. N., Stomberg, R., Raikas, T., Korvenranta, J. & Kekäläinen, U. (1983). *Acta Chem. Scand. A*, **37**, 519–522.
- Dimiduk, D. M. & Perepezko, J. H. (2003). *MRS Bull.* **28**, 639–645.
- Dutour Sikirić, M., Delgado-Friedrichs, O. & Deza, M. (2010). *Acta Cryst.* **A66**, 602–615.
- Frank, F. C. & Kasper, J. S. (1958). *Acta Cryst.* **11**, 184–190.
- Giorgi, A. L. & Matthias, B. T. (1978). *Phys. Rev. B*, **17**, 2160–2162.
- Giorgi, A. L., Matthias, B. T. & Stewart, G. R. (1978). *Solid State Commun.* **27**, 291–294.
- Gokhale, A. B. & Abbaschian, G. J. (1991). *J. Phase Equilib.* **12**, 493–498.
- Kresse, G. & Furthmüller, J. (1996). *Phys. Rev. B*, **54**, 11169–11186.
- Kresse, G. & Hafner, J. (1993). *Phys. Rev. B*, **47**, 558–561.
- Kresse, G. & Joubert, D. (1999). *Phys. Rev. B*, **59**, 1758–1775.
- McMahon, M. I. & Nelmes, R. J. (2006). *Chem. Soc. Rev.* **35**, 943–963.
- Monkhorst, H. J. & Pack, J. D. (1976). *Phys. Rev. B*, **13**, 5188–5192.
- Muller, J. (1980). *Rep. Prog. Phys.* **43**, 641–687.
- Oganov, A. R. & Glass, C. W. (2006). *J. Chem. Phys.* **124**, 244704.
- Okunishi, E., Sawada, H. & Kondo, Y. (2012). *Micron*, **43**, 538–544.
- Perdew, J. P., Burke, K. & Ernzerhof, M. (1996). *Phys. Rev. Lett.* **77**, 3865–3868.
- Perepezko, J. H. (2009). *Science*, **326**, 1068–1069.
- Reuth, E. C. van & Waterstrat, R. M. (1968). *Acta Cryst.* **B24**, 186–196.
- Rosales, I. & Schneibel, J. H. (2000). *Intermetallics*, **8**, 885–889.
- Saini, N. L., Filippi, M., Oyanagi, H., Ihara, H., Iyo, A. & Bianconi, A. (2003). *Phys. Rev. B*, **68**, 104507.
- Sakidja, R., Perepezko, J., Kim, S. & Sekido, N. (2008). *Acta Mater.* **56**, 5223–5244.
- Samson, S. (1965). *Acta Cryst.* **19**, 401–413.
- Shah, D. M. & Anton, D. L. (1992). *Mater. Sci. Eng. A*, **153**, 402–409.
- Shirane, G. & Axe, J. D. (1971). *Phys. Rev. B*, **4**, 2957–2963.
- Steurer, W. (2007). *Z. Kristallogr.* **222**, 259–288.
- Stewart, G. R. (2015). *Physica C Supercond.* **514**, 28–35.
- Tang, H., Van der Ven, A. & Trout, B. L. (2004). *Phys. Rev. B*, **70**, 045420.
- Templeton, D. H. & Dauben, C. H. (1950). *Acta Cryst.* **3**, 261–262.
- Testardi, L. R. (1975). *Rev. Mod. Phys.* **47**, 637–648.
- Tsutomu, I. & Yasushige, F. (1983). *Jpn. J. Appl. Phys.* **22**, 1092–1097.
- Turchi, P., Treglia, G. & Ducastelle, F. (1983). *J. Phys. F Met. Phys.* **13**, 2543–2567.
- Wang, W. K., Iwasaki, H., Suryanarayana, C., Masumoto, T., Toyota, N., Fukase, T. & Kogiku, F. (1982). *J. Mater. Sci.* **17**, 1523–1532.
- Wang, W. K., Wang, Y. J., He, S. A., Huang, J. H., Boyer, J. D., Huang, C. Y. & Iwasaki, H. (1986). *Solid State Commun.* **58**, 285–288.
- Zhu, Q., Jung, D. Y., Oganov, A. R., Glass, C. W., Gatti, C. & Lyakhov, A. O. (2013). *Nat. Chem.* **5**, 61–65.
- Zhu, Q., Oganov, A. R. & Lyakhov, A. O. (2012). *CrystEngComm*, **14**, 3596–3601.